The Astrophysical Journal Supplement Series, 269:11 (18pp), 2023 November https://doi.org/10.3847/1538-4365/acdd69

The Statistical Uncertainties on X-Ray Flux and Spectral Parameters from Chandra ACIS-I Observations of Faint Sources: Application to the Cygnus OB2 Association

J. F. Albacete-Colombo[1,5], E. Flaccomio[2], J. J. Drake[3], N. J. Wright[4], M. Guarcello[2], and V. Kashyap[3]
[1] Universidad de Rio Negro, Sede Atlántica—CONICET, Viedma CP8500, Argentina; albacete.facundo@conicet.gov.ar
[2] Osservatorio Astronomico di Palermo, Palermo, I-90134, Italy
[3] Smithsonian Astrophysical Observatory, 60 Garden St., Cambridge, MA 02138, USA
[4] Astrophysics Group, Keele University, Keele, Staffordshire ST5 5BG, UK
Received 2015 October 15; revised 2016 March 9; accepted 2017 February 2; published 2023 October 25

Abstract

We investigate the uncertainties of fitted X-ray model parameters and fluxes for relatively faint Chandra ACIS-I source spectra. Monte Carlo (MC) simulations are employed to construct a large set of 150,000 fake X-ray spectra in the low photon count statistics regime (from 10 to 350 net counts) using the XSPEC spectral model-fitting package. The simulations employed both absorbed thermal (APEC) and nonthermal (power-law) models, in concert with the Chandra ACIS-I instrument response and interstellar absorption. Simulated X-ray spectra were fit assuming a wide set of different input parameters and *C*-statistic minimization criteria to avoid numerical artifacts in the accepted solutions. Results provide an error estimate for each parameter (absorption, $N_{\rm H}$, plasma temperature, kT, or power-law slope, Γ, and flux) and for different background contamination levels. The distributions of these errors are studied as a function of the 1σ quantiles, and we show how these correlate with different model parameters, net counts in the spectra, and relative background level. Maps of uncertainty in terms of the 1σ quantiles for parameters and flux are computed as a function of spectrum net counts. We find very good agreement between our estimated X-ray spectral parameter and flux uncertainties and those recovered from spectral fitting for a subset of the X-ray sources detected in the Chandra Cygnus OB2 Legacy Survey diagnosed to be association members and that have between 20 and 350 net counts. Our method can provide uncertainties for spectral parameters whenever formal X-ray spectral fits cannot be well constrained, or are unavailable, and predictions useful for computing Chandra ACIS-I exposure times for observation planning.

Unified Astronomy Thesaurus concepts: Computational methods (1965); Astronomical methods (1043); X-ray sources (1822)

Supporting material: animations

1. Introduction

The current generation of flagship soft X-ray telescopes, i.e., Chandra and XMM-Newton, both now over 20 yr old, ushered in a new era of X-ray astronomy thanks to their greatly improved sensitivity and spatial resolution with respect to their predecessors. Large numbers of previously unknown Galactic and extragalactic X-ray sources were discovered and their emission studied in detail. Most of the X-ray sources, however, have been detected with just a few photons, often leaving their astrophysical nature loosely constrained by the X-ray data alone. Quite frequently, there are too few photon counts to distinguish between plausible emission models. Even when the appropriate type of emission model to apply is known with reasonable certainty, the relevant spectral parameters, among the most important of which is the intrinsic absorption-corrected source flux, are often too weakly constrained to allow useful physical inference. The degree to which X-ray emission models can be constrained observationally depends on the instrumental characteristics (the effective area and spectral response), on the source flux, on the shape of the source spectrum, on the foreground and intrinsic extinction, and on the instrumental and astrophysical background contribution to the collected spectrum.

Although standard spectral fitting procedures can provide estimates of uncertainties on model parameters, it would also be useful to have a solid a priori understanding of uncertainties even before the observation is performed, such as when planning new observations. Such estimates are crucial both to determine whether the astrophysical problem at hand is tractable and to choose the best instrument, setup, and exposure time combination. More specifically, given an estimate of the broadband photon flux, common questions are as follows: (i) Will the observed spectra constrain the emission mechanism, i.e., will some of the possible emission mechanisms be rejected on the basis of the spectral shape? (ii) Which parameters can be constrained simultaneously and within a given precision, through spectral fitting with a specific emission model? (iii) To what degree are the estimates of the spectral parameters correlated (e.g., $N_{\rm H}$–kT or $N_{\rm H}$–Γ for thermal or nonthermal emission subject to interstellar absorption)?

Unfortunately, no appropriate tool to address these questions is available, to our knowledge, and resorting to Monte Carlo (MC) simulations for each specific case may not be practical and can be overly time-consuming. As a result, the preparation of new observing campaigns and the proposal selection process are too often based on previous more or less relevant experiences or qualitative assessment, rather than on firm quantitative estimates. Some of these questions were discussed

[5] External postdoctoral fellow in the visiting programmer of CONICET.

by Maggio et al. (1995) for the case of the ROSAT PSPC detector, using MC simulations to investigate the dependence of fit quality with counting statistics and, in particular, the ability to discern isothermal from multitemperature plasma emission (e.g., one vs. two thermal components). With the increased effective area and reduced background of modern-day X-ray telescopes, the occurrence of sources detected with a handful to a few tens of photons has increased dramatically with respect to the times of ROSAT. Exploiting the information contained in low-count detections, as well as understanding the limitations, has thus become more pressing than ever.

In this contribution, we present the results of extensive MC simulations intended to answer the above questions for the rather common case of faint X-ray sources with thermal and/or power-law emission spectra. One such case is the observation with Chandra ACIS-I of the young OB association Cygnus OB2, inevitably also containing a population of background sources, mostly extragalactic active galactic nuclei (AGNs), and a population of foreground sources, mostly normal stars. Young stars are expected to have rather energetic thermal emission spectra ($kT \sim 2$–4 keV) and, in the case of Cyg OB2, to be considerably absorbed by both their parent cloud and interstellar material. Foreground stars are expected to show softer thermal spectra subject to less absorption. Extragalactic sources will be characterized by mostly non-thermal power-law spectra, with, on average, harder spectra than young stars. Although it would be desirable to distinguish among these three cases from the X-ray spectra alone, in practice, for low-count sources, this is often not possible.

In the following, we use MC simulations to determine the precision with which X-ray source fluxes and model parameters can be determined from Chandra ACIS-I observations, as a function of the model parameters, absorption, number of photon events, and background level (the latter being mostly a function of exposure time and source position in the focal plane). The paper is structured as follows: In Section 2, we detail our MC procedure for thermal and nonthermal emission models and our exploration of the parameter/count-statistic/background space. We also discuss the effects on uncertainties of rather technical aspects of spectral fitting, such as the way spectra are rebinned before fitting. In Section 3, we make use of our MC simulations to estimate, in the low-background regime, the uncertainties on unabsorbed X-ray fluxes and model parameters for each point on our 3D simulation grid (with axes: source counts, source extinction, parameterized by the hydrogen column density $N_{\rm H}$, and a single spectral parameter for the source, kT for thermal models or Γ for nonthermal ones). We also discuss how these results are interpolated to estimate uncertainties at any point within the grid. In Section 4, we extend the results presented in Section 3 to sources with nonnegligible background. Section 5 compares our a priori estimates of uncertainties with the results of X-ray spectral analysis of low-count stellar sources detected in the Cyg OB2 star-forming region as part of the Cygnus OB2 Chandra Legacy Survey, presented as an X-ray catalog of sources (Wright et al. 2023a, 2023b) and an accompanying catalog of optical and infrared counterparts (Guarcello et al. 2023). Finally, in Section 6 we briefly discuss the impact of our work on future science and, in particular, for planning new observations, i.e., to compute exposures times using the ACIS-I Chandra camera.

In the Appendix, as an example, we show a set of bidimensional maps that illustrate the application of our results to ACIS-I source spectra.

2. X-Ray Spectral Simulations

We decided to focus on two of the most commonly used X-ray emission models: thermal emission from an optically thin plasma and power-law spectra, as described by the APEC (Smith et al. 2001) and POWERLAW models within the XSPEC[6] (Arnaud 1996) parameter estimation code. The spectral shape of both models is fully described by a single parameter, the plasma temperature, kT, for APEC and the power-law index, Γ, for POWERLAW. A normalization that may be expressed in terms of energy flux, photon flux, or count rate (all in a given band) completes the description of the model. The APEC model assumes the solar mixture of heavy elements compiled by Anders & Grevesse (1989). The intrinsic source emission was absorbed using the photoelectric absorption model TBABS, characterized by the equivalent hydrogen column depth $N_{\rm H}$.

The observed ACIS-I spectrum of a point source may be fully specified by the incident spectrum (assumed specified by kT or Γ for thermal or nonthermal emission, respectively, as noted above), $N_{\rm H}$, a normalization factor, the instrumental response, i.e., effective area and spectral response, and the background contribution to the collected spectrum, of both instrumental and astrophysical origin. In the following we will make the simplifying assumption that, for any given incident source spectrum, the quality of the observed spectrum, and thus the uncertainties we can associate with model parameters after spectral fitting, will only be influenced by the number of source and background photons. In other words, we will assume that the spectral response function and the *shape* of the effective area versus energy function are the same for all sources. While this is not strictly true—the ACIS-I effective area depends weakly on the off-axis angle, for example—any departures from this assumption are expected to have only a second-order influence on the precision of derived spectral parameters.

In this section, we will further assume that the background is small, not null, typical of an almost on-axis source for which the point-spread function (PSF), and thus the photon extraction area, is small. See details in Section 2.1. This restriction will be lifted in Section 4. The response matrix file (RMF) and ancillary response file (ARF) functions were also chosen to be appropriate for the same source. We will therefore only vary three parameters in the spectral simulations, $N_{\rm H}$, kT, or Γ, and the number of source counts detected in the 0.5–8.0 keV band, net_cnts. In a real observation, the latter quantity is the product of the source photon flux, the exposure time, and the effective area.

Our simulation domain is defined by grids ($N_{\rm H}$, kT/Γ) that encompass the parameter values of most astrophysical sources, as derived from Chandra and XMM-Newton observations. In particular, for thermal models our grid is defined by six values of $N_{\rm H}$ ($(0.1, 0.33, 1.0, 3.3, 10, 33.3) \times 10^{22}$ cm^{-2}) and eight values of kT (0.5, 0.8, 1.2, 2.0, 3.0, 4.0, 6.0, 10.0 keV) for a total of 48 combinations. For nonthermal models, we adopt the same $N_{\rm H}$ values and five values for the power-law index Γ (1.0, 2.0, 3.0, 4.0, 5.0), for a total of 30 combinations.

For each point on these parameter grids, we run simulations adjusting the model normalization so as to have, on average,

[6] http://heasarc.gsfc.nasa.gov/docs/xanadu/xspec/index.html

spectra with a given number of counts, net_cnts, in the 0.5–8.0 keV band. Nineteen values are adopted for net_cnts: 10, 15, 20, 25, 30, 35, 40, 50, 60, 70, 80, 90, 100, 120, 140, 160, 200, 240, and 350. The number of points in our 3D grids thus amounts to 624 and 390 for thermal and nonthermal models, respectively. The number of simulations performed for each grid point is chosen so as to reduce random fluctuations on the distribution of the output parameters to an acceptable level (see below). A total of about 150,000 MC simulations were performed to probe the parameter estimation uncertainties themselves. Another set of about 500,000 MC simulations were performed to understand the effect of the background contribution to the uncertainty estimation (see Section 4).

All the MC simulations were performed with XSPEC v.12.8 (Arnaud 1996), using our own *tcl* script, CIAO (v4.5) commands, and IDL (© Exelis Inc.) routines. Simulated spectra, as would be observed by ACIS-I, were created starting from our input spectral model, ARF, RMF, and background files (see above), using the FAKEIT XSPEC command, including statistical Poisson fluctuations. Spectra were then rebinned as we would do for real source spectra before fitting (see Section 2.1), and spectral fitting was performed following the same procedure we follow for real data (see Flaccomio et al. 2023). In particular, we adopt the Cash statistic (Cash 1979; *C*-stat), which is more suitable than χ^2-based methods in the regime of small numbers of photon events, and choose as our final best-fit model the one with the minimum *C*-stat value. We repeat each fit starting from several initial values of the model parameters $N_{\rm H}$ and kT/Γ to reduce the chances of the model finding a local minimum in *C*-stat space.

2.1. The Role of Binning in Spectral Fitting

An interesting point to address before we proceed is how the binning of X-ray spectra along the energy axis affects the outcome of the fitting process and, in particular, the uncertainties on the model parameters. A good measure of uncertainty can be obtained from the relative error of a given parameter, which can be computed as the ratio between the fit result and the known input value defined in the simulated spectra. If bin sizes and/or method have an effect, we should determine, and use, an optimal strategy.

We tested two spectral binning approaches: (i) the common *minimum counts* method, in which photons are grouped so that each bin includes at least the specified number of detected photons, as implemented by the GRPPHA command; and (ii) the *minimum signal-to-noise ratio* (S/N) method, in which photons are grouped so as to reach a minimum S/N per bin, where the S/N estimation takes the background photons into account. In particular, the reference background was taken to be that of a point source located 3.′16 off-axis: the background spectrum is defined by ∼100 photons in the 0.5–8.0 keV band, which must be scaled down to 0.9 photons in the source extraction area containing 90% of the PSF power. The latter method was used as implemented in the ACIS Extract/TARA IDL package (Broos et al. 2010); it has the added advantage that the user can specify the low- and high-energy boundaries of the first and last bins. This is useful when fitting spectra in a fixed energy band (in our case 0.5–8.0 keV) because, by choosing the proper boundaries, one can efficiently exclude photons with energies outside that band, as opposed to having to exclude bins overlapping with the limit boundaries and that likely contain

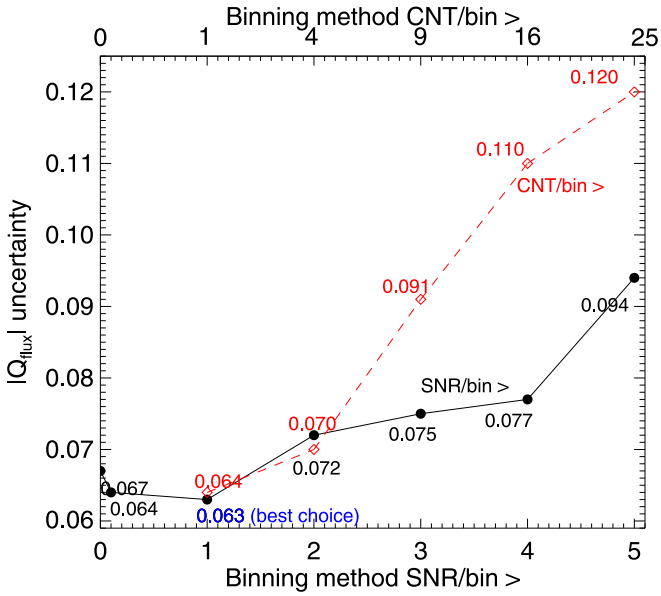

Figure 1. The relative 1σ quantile flux errors, $|Q_{\rm flux}|$ (see text for the formal definition), as a function of either the minimum number of counts per bin (red points, upper *x*-axis) or the minimum S/N per bin (black points, lower *x*-axis) in X-ray spectral fitting simulations. The errors were computed from a set of 1000 simulations for each binning strategy. The minimum relative error occurs whenever simulated X-ray spectra are fitted with an S/N/bin > 1. The same result is derived from the analysis of relative errors of other spectral model parameters.

photons with energies in the acceptable range. This is particularly relevant for low-count sources.

We conducted our numerical experiments on binning using a specific spectral model from our grid, an absorbed optically thin thermal plasma spectrum with $N_{\rm H} = 10^{22}\,{\rm cm}^{-2}$, $kT = 2.0$ keV, and normalization set to result, on average, in spectra with 200 net source counts. We do not expect our conclusions to depend critically on this choice. A set of 1000 simulations was run for each binning method, i.e., for S/N > 1, 2, 3, 4, and 5, and for $\rm nphot_{min} > 1$, 4, 9, 16, and 25.[7] For each set of simulations we derive the relative uncertainties to be expected from the spectral fit of a single spectrum for an unabsorbed flux (0.5–8.0 keV), $N_{\rm H}$, and *kT*.

We compute the relative error of a given *Y* spectral quantity ($N_{\rm H}$, kT/Γ, or flux) as the ratio between the parameter best-fit value and the model input value. Then, the 1σ quantile error (Q_Y) is an indicator of the uncertainty by taking the $\pm1\sigma$, i.e., 16% (Q_Y^-) and 84% (Q_Y^+) quantiles computed from the cumulative distribution of the relative errors of *Y*. Hereafter we call such a quantity a "*Q* uncertainty." Its respective errors were calculated in order to ascertain the significance of any effect of binning parameter/method on the uncertainties by using the Maritz–Jarrett method (Hong et al. 2004).

Figure 1 shows the *Q* uncertainty on $F_{\rm X}$, which were computed from a set of 1000 simulations for each binning strategy. The *Q* uncertainties here are represented by the mean of the absolute value of the flux error quantiles, $|Q_{\rm flux}| = (|Q^+_{\rm flux}| + |Q^-_{\rm flux}|)/2$. The figure demonstrates that *Q* uncertainties on best-fit parameters do actually depend on binning. The *minimum counts* method (CNT/bin) produces the

[7] Barring other differences in the binning algorithm, critically the choice of limits for the first and last bins, the two sets of values imply the same binning for the case of zero background, since $\rm S/N = nphot^{1/2}$.

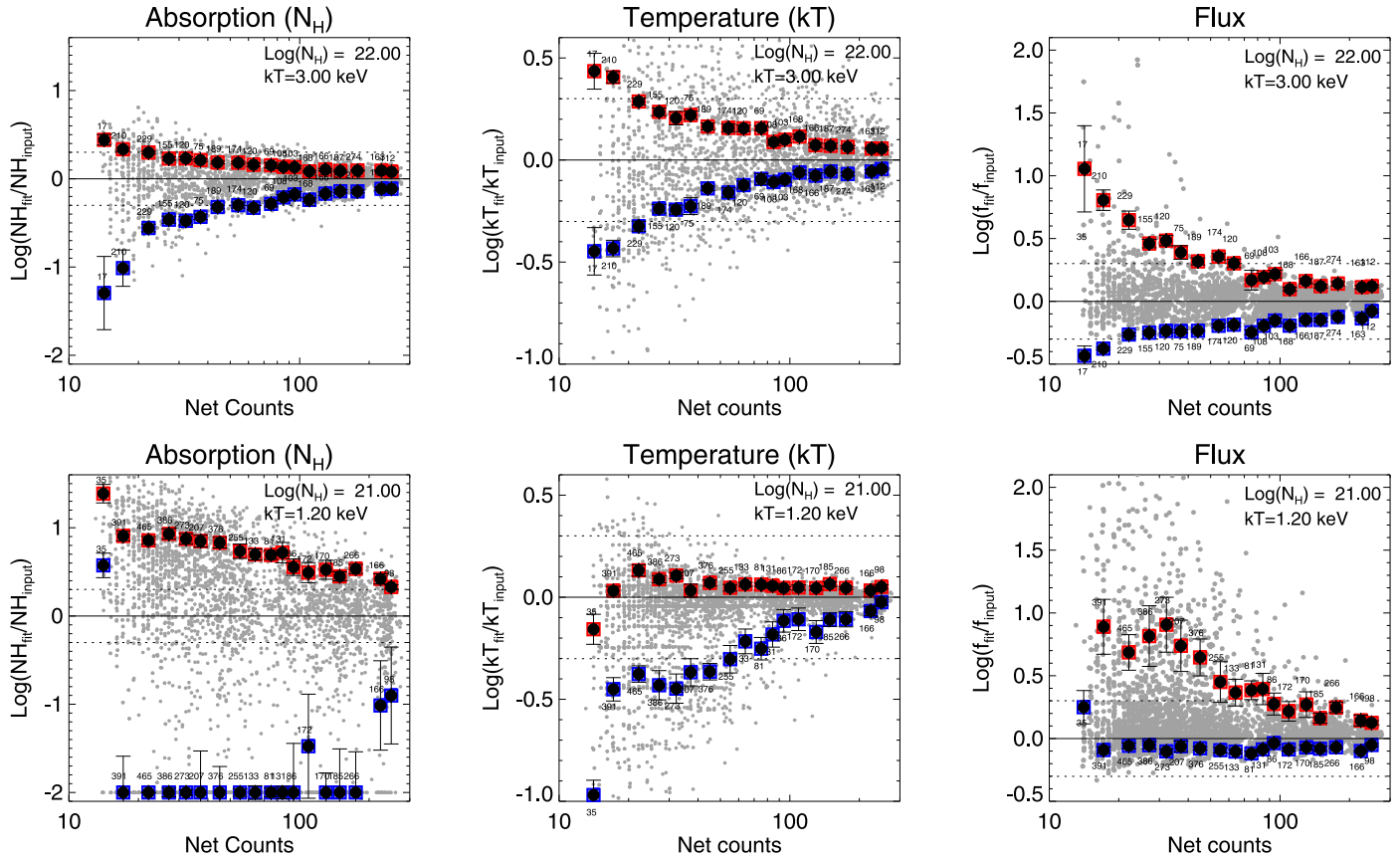

Figure 2. The relative errors in $N_{\rm H}$, kT, and flux as a function of the input net counts imposed on the spectral simulations. The top panels correspond to a spectral model grid point $\log(N_{\rm H}) = 22.0$ and $kT = 3.0$ keV, and the bottom panels correspond to a model with $\log(N_{\rm H}) = 21.0$ and $kT = 1.2$ keV. The red and blue boxes refer to the Q uncertainty computed for the relative error distributions (gray circles) for each incremental range in photon counts in which we simulate the spectra. The numbers next to these points indicate the number of simulations included in each respective bin. We point out that relative errors for $N_{\rm H}$ in the bottom middle panel artificially bottom out at an $N_{\rm H}$ value a factor of 100 lower than the input value for cases of less than about 100 net source counts. This numerical conditioning is imposed in order to avoid unconstrained lower limit values of $N_{\rm H}$ for low column density cases (see also Section 3).

largest uncertainties, particularly for bins with counts/bin > 4, while the *minimum S/N* method (S/N per bin) for S/N/bin > 1 is the best choice and less affected by statistical bias in the fitting procedure. For large bins the superiority of the S/N method is likely accentuated by the fact that it does not waste photons, while a growing number of photons in the bin overlapping with the energy limits are discarded in the former case. Moreover, in the case of the *minimum counts* method, we find that the median values of the best-fit parameters diverge from the synthetic spectrum input values as the binning increases, signaling that potentially biased results might result from such a procedure.

In summary, these numerical results indicate that binning spectra so that S/N/bin > 1 produces unbiased best-fit values with minimal uncertainties. This is thus the binning strategy we adopt in the work that follows.

3. Analysis of Uncertainties

The outcome of our extensive set of MC simulations is a large collection of best-fit spectral parameters from the fitting of simulated spectra. We will focus on $N_{\rm H}^{\rm fit}$, $kT^{\rm fit}/\Gamma^{\rm fit}$ (for thermal/nonthermal models), and, importantly, $F_{\rm X}^{\rm fit}$, the absorption-corrected X-ray flux, and study how the Q uncertainties on the determination of these parameters depend both on photon statistics and on their values.

In Figure 2, we show, for two model spectra, the runs of best-fit $F_{\rm X}$, $N_{\rm H}$, and kT as a function of the number of source counts. Also shown are the $\pm 1\sigma$ quantiles (Q_Y^- and Q_Y^+) computed for source net counts in the range 10–350. The top and bottom panels refer to a relatively hard and highly absorbed thermal source ($N_{\rm H} = 10^{22}$ cm^{-2}, $kT = 3.0$ keV) and to a softer, less absorbed source ($N_{\rm H} = 10^{21}$ cm^{-2}, $kT = 1.2$ keV), respectively, illustrating how model dependent our results are. We note in particular difficulties in constraining the absorption for the latter, less absorbed model, for which lower limits to the $N_{\rm H}$ parameter were often not restricted by the data for cases in which there were fewer than 100 net counts. In these cases, the blue squares representing the lower quantile limits are set to the lower limit of the allowed range we specified in the XSPEC fitting procedure —a factor of 100 less than the input value. This lack of sensitivity to low $N_{\rm H}$ values occurs because of the limited soft X-ray response of ACIS-I; this has been eroded since launch by the gradual buildup of a molecular contamination layer that attenuates low-energy X-rays (e.g., O'Dell et al. 2013). This limitation places a constraint on the range of validity of our results in the sense that uncertainties in $N_{\rm H}$ will be strictly accurate for $N_{\rm H} \gtrsim 10^{21}$ cm^2. For lower column densities both the $N_{\rm H}$ and unabsorbed flux uncertainties are subject to systematic error, the latter being affected because it is dependent on the former. We return to this briefly in the verification of our method in Section 5.

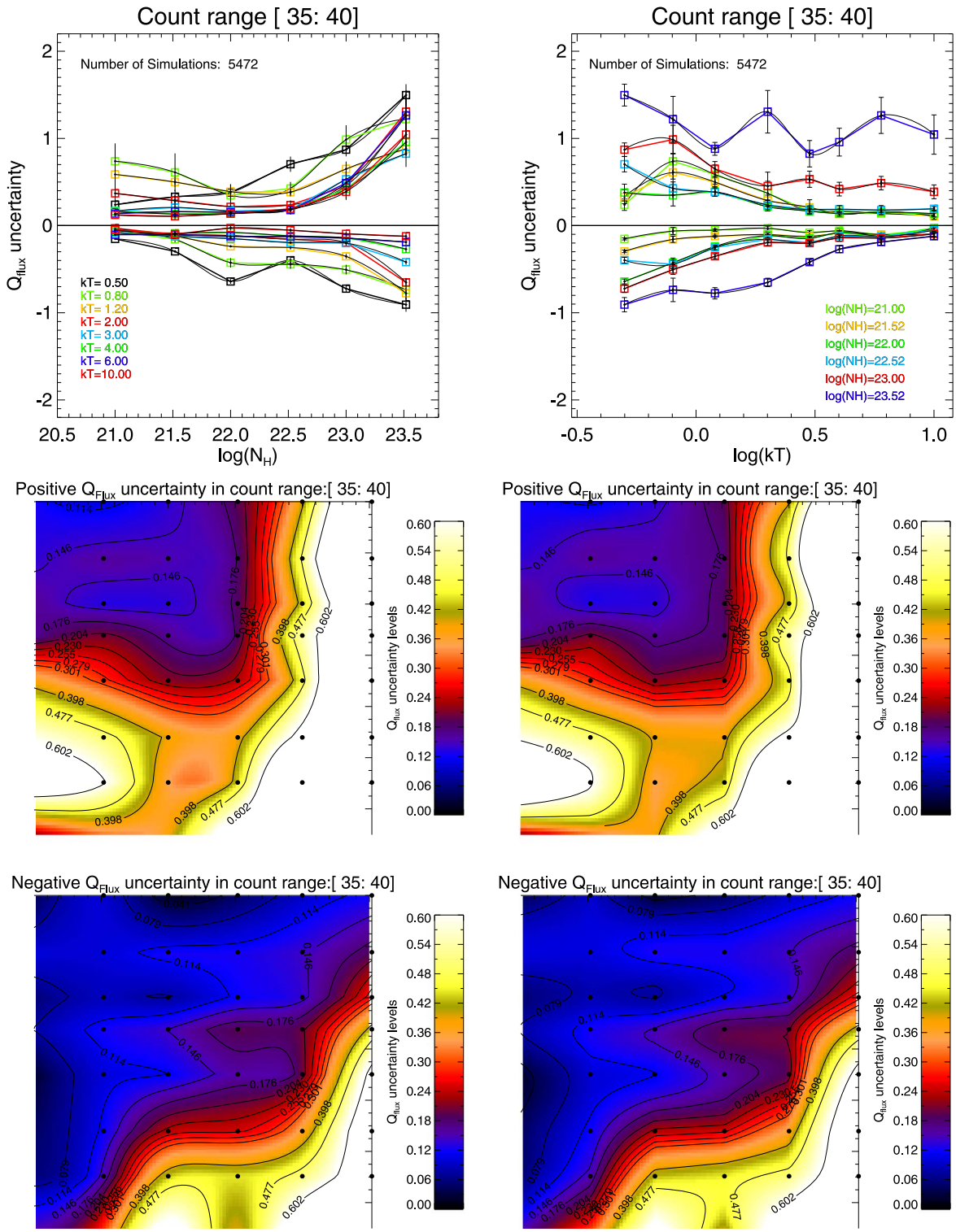

Figure 3. Flux Q uncertainty as a function of $N_{\rm H}$ and kT. The top left panel shows a set of eight different kT curves interpolated using a cubic spline function for MC-simulated spectra in the range of 35–40 photons. The $Q_{\rm flux}$ uncertainty is shown in the left column as 2D bidimensional maps, which was computed from the kT (y-axis) curves followed by a linear interpolation along the orthogonal ($N_{\rm H}$) direction (x-axis). The top right panel shows the median $Q_{\rm flux}$ uncertainties (boxes) for the six different $N_{\rm H}$ curves also interpolated by a cubic spline function and for the same range of photon counts. The rest of the panels in the right column show the $Q_{\rm flux}$ uncertainty as a bidimensional map computed in an inverse interpolation order, i.e., along the kT direction. Note that for the 2D maps both columns are essentially the same, with only very small differences, which suggests that no interpolation artifacts were created in our numerical treatment of Q uncertainties.

Another useful way to visualize our results is illustrated in Figure 3 (top and bottom left panels). Here we show, for models with total counts in a given range (in this case 35–40 counts), the flux uncertainties/quantiles as a function of input kT for different input values of $N_{\rm H}$ (top panel) and input $N_{\rm H}$ for different input values of kT (bottom panel). These figures illustrate that the dependence of uncertainties on model parameters is nontrivial and cannot easily be approximated analytically.

The 3D thermal and nonthermal grids of simulations also allow us to easily view aspects of the results in two dimensions (three dimensions is also of course possible, but it is challenging to interpret). Also illustrated in the middle and right panels of Figure 3 is an example of how contour maps of the 2D dependence of the positive and negative 1σ relative flux uncertainties depend on $N_{\rm H}$ and kT for the case of thermal spectra with 35–40 counts. To avoid discontinuous artifacts resulting from the limited sampling of our grid, these maps were produced by interpolating within the grids using a cubic spline function. We tested this method by interpolating both in $N_{\rm H}$ for fixed kT values (top middle and right panels) and in kT for fixed $N_{\rm H}$ values (bottom middle and right panels). The two approaches are in very good agreement, indicating that the $\log(N_{\rm H})$–$\log(kT)$ space is well mapped and that the approach is free from significant numerical instability or bias. The contour curves in Figure 3 were computed for logarithmic relative error values equal to log([1.001, 1.1, 1.2, 1.3, 1.4, 1.5, 1.6, 1.7, 1.8, 1.9, 2.0, 2.5, 3.0, 4.0]).

At this point, we are able to give a full description of the Q uncertainty for any value of $N_{\rm H}$, kT, or Γ, as well as X-ray flux, for a given discrete range of net counts (see the Appendix). However, as we mention in Section 2, the X-ray spectral simulations were performed by adopting a negligible background fraction in the spectra. Obviously, these results cannot be applied to those sources that suffer from higher background contributions. For on-axis observations with Chandra ACIS-I, for which the PSF is very compact, background can often be very low compared with source counts. However, the PSF angular size increases with increasing off-axis angle,[8] and consequently the fraction of the photon events that comprise an extracted source spectrum that can be attributed to background also increases. The background contribution can be particularly significant for large off-axis angles ($\gtrsim 3'$). We address this problem in the next section.

4. How Background Photons Affect the Q Uncertainty

The results presented in Sections 2 and 3 correspond to the case of sources with negligible background contamination, i.e., a background fraction less than 0.01. As noted above, this is generally not the case for Chandra, or many other X-ray observations, for which background events can be a significant or even dominant fraction of the extracted signal. High background contributions can potentially mask or bias the true nature of source X-ray spectra, make spectra noisy, and compromise their interpretation and the ability to constrain spectral parameters in astrophysical modeling. In this section, we study this effect by means of further extensive MC simulations of background-affected spectra.

As before, the main goal is to estimate the dependence of the uncertainty of fitted spectral parameters on the intrinsic X-ray emission source model and the net photon counts of the spectra. We constructed a set of simulations based on eight different thermal and nonthermal X-ray emission models, simulated for different numbers of source and background counts. The background fraction of the simulations ranged from 0.001 to the limiting case of 1 (corresponding to a spectrum composed of 100% background photons). We adopted RMF, ARF, and background (BKG) files that correspond to a set of 100 X-ray sources randomly distributed over the field of view of the ACIS-I Chandra ObsID 4511 of the Cygnus OB2 association (see Albacete Colombo et al. 2007, for further details of the observation).

[8] See http://cxc.harvard.edu/proposer/POG/html/chap4.html for details.

Table 1
X-ray Emission Models Used to Investigate the Effect of Background Contamination Fraction in the Determination of Q Uncertainties of Spectral Parameters from Simulated Spectra

Model No.	Thermal			Nonthermal		
	$N_{\rm H}$ ($\rm cm^{-2}$)	kT (keV)	$N_{\rm sims}$	$N_{\rm H}$ ($\rm cm^{-2}$)	Γ	$N_{\rm sims}$
1	1.0×10^{22}	3.0	32,017	10^{21}	1.0	26,031
2	0.1×10^{22}	1.2	35,779	10^{21}	3.0	29,467
3	0.1×10^{22}	3.0	31,413	10^{21}	5.0	29,304
4	0.33×10^{22}	3.0	49,918	10^{22}	1.0	21,967
5	3.3×10^{22}	1.2	50,159	10^{22}	3.0	15,269
6	1.0×10^{22}	1.2	48,968	10^{22}	5.0	23,032
7	33.0×10^{22}	3.0	46,859	10^{23}	1.0	22,730
8	10.0×10^{22}	3.0	31,762	10^{23}	3.0	18,776
9	0.1×10^{22}	5.0	45,730	10^{23}	5.0	7172
10	0.33×10^{22}	5.0	44,960	– –	– –	
11	1.0×10^{22}	5.0	41,042	– –	– –	
12	3.3×10^{22}	5.0	34,020	– –	– –	
13	10.0×10^{22}	5.0	45,116	– –	– –	
14	33.0×10^{22}	5.0	49,918	– –	– –	

Due to the additional dimension of background fraction, we covered a more limited segment of the $N_{\rm H}$–kT plane than in the zero background grid employed in Section 2. Thermal and nonthermal models were computed for a set of temperatures and/or Γ index values that are listed in Table 1 and also illustrated in Figure 4. This amounted to a set of 14×100 (thermal case) simulations for background fractions from 0.001 to 1 and for total events numbering 20, 30, 100, and 300 photons.

In the left panel of Figure 4, we show the distribution of fit solutions for each model and for the different net counts in the spectra and background contamination fractions. At low absorption, the retrieved $N_{\rm H}$ uncertainty is greater than that in temperature, while the opposite behavior occurs when $N_{\rm H}$ becomes large, leading to a poor determination of temperature. This behavior arises simply because of the way the spectral "lever arm" acts: at low $N_{\rm H}$, there is little energy range over which the spectrum is significantly affected by absorption and purchase on $N_{\rm H}$ is weak—as in the case of unconstrained $N_{\rm H}$ lower limits noted in Section 3 above; conversely, there is a large energy range available to discern the spectral shape characteristics that are affected by temperature. At high $N_{\rm H}$, the opposite is true. Furthermore, uncertainty in temperature grows at higher temperatures because of the limited broadband energy range available for our spectral fit. The spectrum tends to flatten out within the 8.0 keV bound we adopt; at higher energies where the temperature discrimination power largely lies for the hotter models, the ACIS-I effective area declines rapidly.

Closer inspection of the left panel of Figure 4 reveals some striation in the distributions of best-fit parameters, indicating that certain quantized values of temperature are slightly preferred over others. These artifacts result from the fits to spectra with low numbers of counts ($\leqslant 30$ photons), and the preferred temperatures are those of the plasma radiative loss model temperature grid. They occur when the uncertainties on the spectral fit are large, much larger than the grid quantization. This apparent fit bias only affects a very small fraction of the total and does not impose any bias on fit quantiles because the

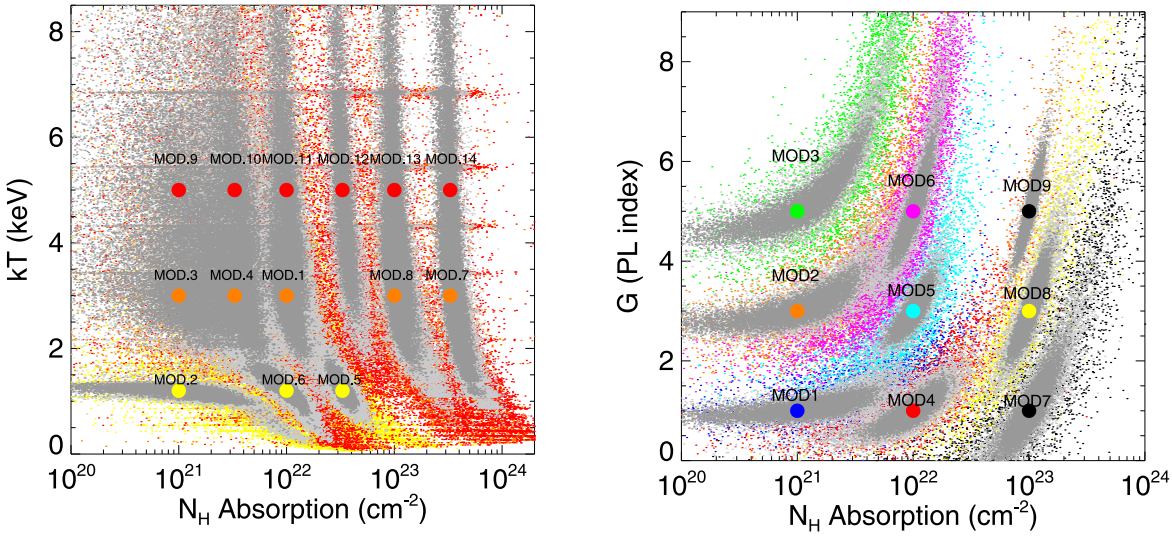

Figure 4. Left: $N_{\rm H}$–kT space of solutions from ∼ 500,000 MC simulations for different models, net counts, and background fractions. The different colors refer to the simulated thermal spectra at the 14 different $N_{\rm H}$–kT input values (large colored circles). Small colored circles are those that correspond to MC simulations for 20 and 30 net counts in the spectra. Light-gray and darker-gray circles show the MC simulations for net counts of 100 and 300 photons in the spectra, respectively. The clustering of points giving rise to a small degree of horizontal striping along the direction of the kT axis corresponds to slightly biased spectral fit solutions that mostly occur for MC simulations with 20 and 30 net counts (see text). Right: a similar illustration of a total of ∼192,000 nonthermal MC simulations for different $N_{\rm H}$–Γ models and background fractions.

quantization effect is on a scale smaller than parameter estimation uncertainties.

A similar procedure to that for thermal models was followed to compute nonthermal models. A 3×3 grid of power-law indices ($\Gamma = 1,\ 3,\ 5$) and absorbing column densities ($N_{\rm H} = 10^{21},\ 10^{22},\ 10^{23}$) was adopted, amounting to 9×100 MC nonthermal simulations for background fractions in the range 0.001–1, and for 20, 30, 100, and 300 photons (see the right panel of Figure 4). The striation effect discernible for the thermal model fits does not occur for nonthermal models because the spectral model itself is analytic and not stored in quantized, tabulated form.

In order to get a quantitative estimate of the uncertainty in best-fit spectral parameters, we compute their relative errors and respective quantiles as a function of the background fraction. Uncertainties correlate linearly with the background fraction of the simulated spectra, being well described by a function of the form

$$\mathrm{Err(bkg\_frac,\ cnt)} = A\mathrm{(cnt)} \times \mathrm{bkg\_frac} + \mathrm{B(cnt)}. \quad (1)$$

The coefficients of such a relationship are not the same for all spectral models even if they have the same net numbers of counts in the simulated spectra. They depend on the emission characteristics of the source, as well as the S/N of the simulations. We evaluated the linear dependence of all 14 thermal and 9 nonthermal models and computed the explicit dependence of Q on bkg_frac. In Table 1, we list the parameters of the background-affected spectral models to map $N_{\rm H}$–kT or $N_{\rm H}$–Γ planes, as well as the total of simulations performed for each one. Of the coefficients A (the slope) and B (the intercept), the latter agrees with the 1σ quantile error estimation for MC simulations of spectra in which the background fraction is negligible or zero (bkg_frac < 0.01). We thus can rewrite Equation (1) as

$$\mathrm{Err(bkg\_frac,\ cnt)} = A\mathrm{(cnt)} \times \mathrm{bkg\_frac.} + Q_0\mathrm{(cnt)}. \quad (2)$$

In the Appendix we list explicit A(cnt) coefficients computed from the uncertainty curves for 20, 30, 100, and 300 photons in background-affected MC-simulated spectra. Such coefficients represent the change of the uncertainty estimation Q_0 due to the influence of background photons in the net counts of the X-ray spectra. The most straightforward way to get the adequate A coefficient for a given X-ray source is by choosing the most representative model for the true source X-ray spectrum.

We can linearly interpolate within the grid of results to obtain bidimensional planes of the uncertainties in any given parameter as a function of background fraction for a given number of total counts between 20 and 300. As an example, in Figure 5 we show how the uncertainty in X-ray flux increases with the background fraction and how it is more tightly constrained as the net counts in the spectra increase. The thermal "model 1" ($N_{\rm H} = 10^{22}$ and $kT = 3.0$ keV; see Figure 5) was chosen as the example for this figure and corresponds to the most representative model of the sources in the Cyg OB2 association (which are mostly T Tauri stars; Albacete Colombo et al. 2007; Flaccomio et al. 2023). We discuss the Cyg OB2 case in more detail in Section 5.

5. Testing Uncertainties of X-Ray Model Parameters for Faint Cyg OB2 Sources

One main motivation of this work is to estimate the uncertainties on luminosities and spectral parameters expected for sources yet to be observed, based on the anticipated ACIS-I Chandra X-ray spectrum. However, another use is to cross-check, or even calculate, the uncertainty obtained from the fitting process and to give rough estimates in those cases in which the calculation of uncertainties fails formally (e.g., when the ERROR command in XSPEC fails owing to numerical issues). As a first application and verification of our method, we use real data and spectra that have been extracted as part of the Cygnus OB2 Chandra Legacy Survey. In this context, our aim is (i) to give spectral fit constraints from our quantile method for Cyg OB2 sources and (ii) to compare the uncertainties in the X-ray spectral parameters for faint sources

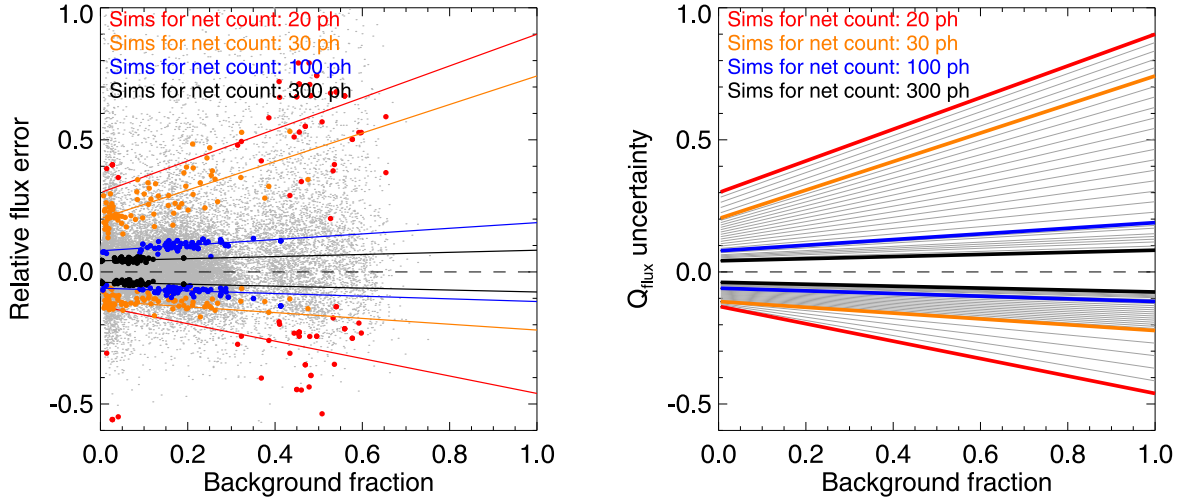

Figure 5. The left panel illustrates curves fitted to the relative flux error as a function of the background fraction for the thermal model 1 ($N_{\rm H} = 1.0 \times 10^{22}$, $kT = 3.0$) according to MC simulations containing 20 (red), 30 (orange), 100 (blue), and 300 (black) net photons in the spectra, respectively (see text). Large colored circles in the panel are the quantile uncertainties for flux. The relationship between the flux uncertainty and background fraction is clearly quite linear. The right panel illustrates the synthesis of the fits to the data of the left panel. The whole set of interpolated curves for the rest of the model parameters investigated and for each of 14 models was computed but not shown here. The same numerical treatment was performed for nonthermal models and for all spectral parameters.

with those results obtained from noninteractive spectral fits presented in Flaccomio et al. (2023).

Following results of the analysis presented by Wright et al. (2023a), a large fraction of the Cyg OB2 sources have been detected at large off-axis angles with ACIS-I. As we have noted above, the PSF degradation of the ACIS-I detector with increasing off-axis angle means that the relative contribution of background photons to source events can be relatively large, which can affect the way in which spectral fitting converges, as well as the uncertainty in the computed spectral solution. In fact, of the 7924 Cyg OB2 sources, just 10 have background fractions less than ∼0.01. The median of the distribution of background fractions is ∼0.36, with some background fractions being as high as 0.9. Thus, if we want to get an unbiased 1σ quantile error estimation, it is strictly necessary to include the background dependency while accounting for the different X-ray emission characteristics of the sources. We employ a set of nine different optically thin thermal plasma models that in the kT–$N_{\rm H}$ plane represent the range in the uncertainty of parameters and flux as a function of the different background fractions (see Figure 6). This procedure allows us to get a much more precise estimate of the influence of the background on parameter uncertainties than we would be able to from the use of a single average model.

The complete catalog of Cyg OB2 sources in the survey comprises a total of 7924 X-ray objects (Wright et al. 2023a). Of these, 4975 have less than 20 net photons, i.e., about 62% of the whole source sample. Flaccomio et al. (2023) have performed spectral fitting of X-ray spectra for sources with more than 20 and less than 350 counts, and if we restrict the sample to this range, we get a total of 2755 sources for which X-ray spectral fits could give an error estimation for the model parameters and flux. We further limit ourselves to X-ray sources that were classified as members of the association (Kashyap et al. 2023) and whose X-ray spectral fitted parameters are in the range of $N_{\rm H} = 1 \times 10^{21}$ to 3.3×10^{23} and $kT = 0.5$–8 keV. This subsample contains 1718 sources and corresponds to 20% of the entire sample of Cyg OB2 members.

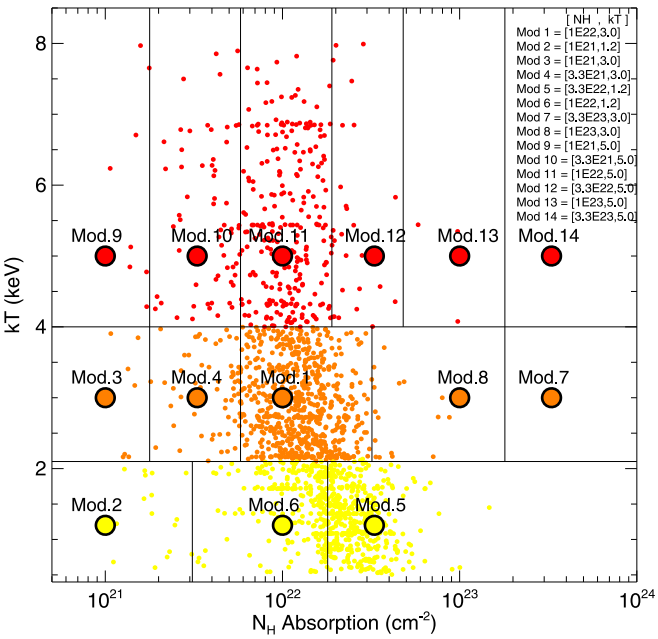

Figure 6. The kT–$N_{\rm H}$ plane for parameter values obtained from X-ray spectral fits to Cyg OB2 in sources having a signal strength in the range of 20–350 net photons. The nine colored models are those used to compute the influence of the different background fractions in the determination of uncertainty for a range of spectral parameters.

5.1. Comparing Errors from Spectral Fits with Quantile Estimates

In this subsection we study the goodness of our method in the determination of uncertainties of the X-ray parameters computed from spectral fits. To do that, we need to account for two approaches: (i) to compute the fit error of a given parameter (fit_err) via the XSPEC error command, which consists in the 1σ error computed from the covariance matrix in the spectral fits of Cyg OB2 stars (see Flaccomio et al. 2023); and (ii) to determine the respective Q uncertainties computed from our 2D quantile maps corrected by the influence of the individual X-ray background fraction of the Cyg OB2 sources.

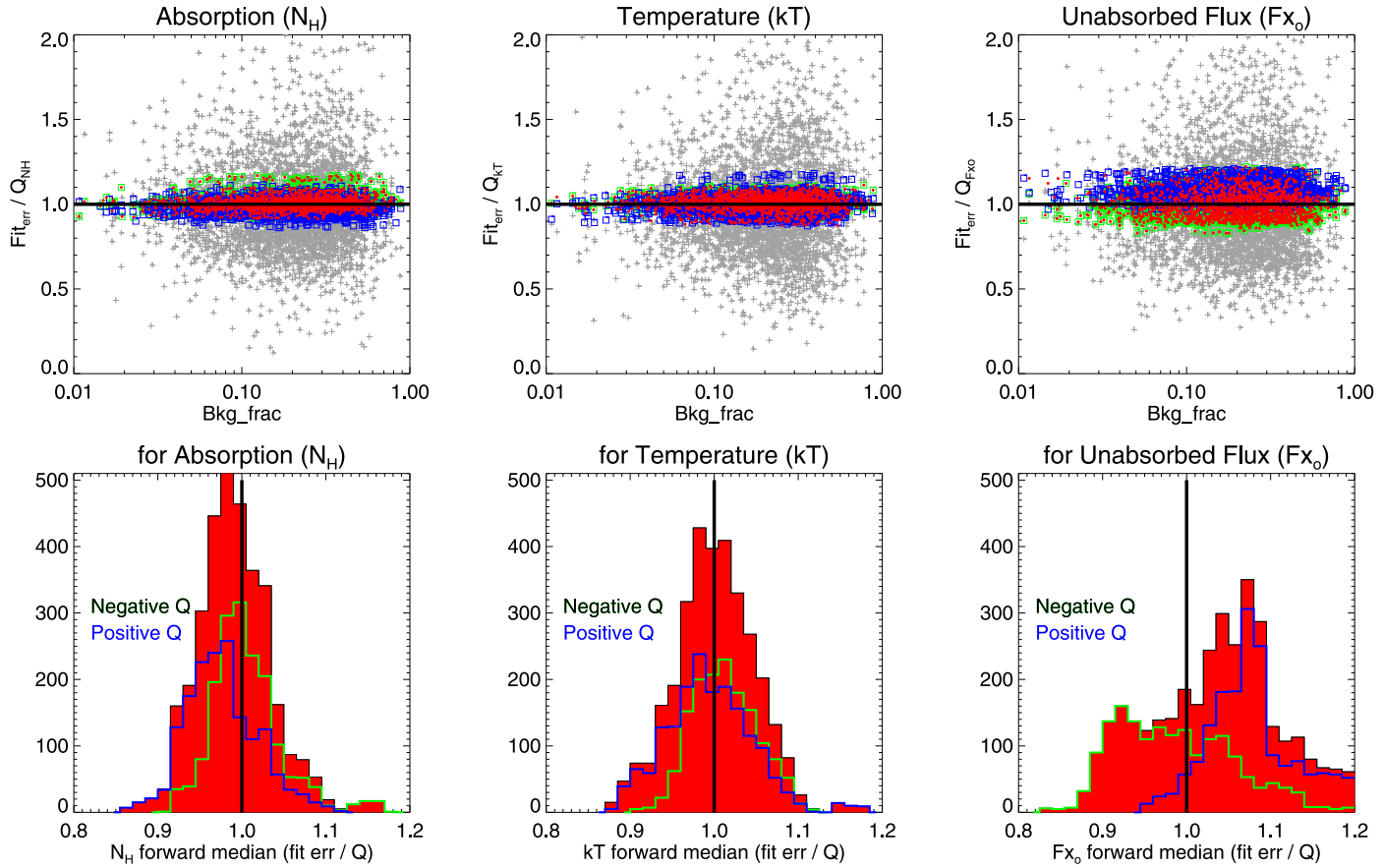

Figure 7. Top: the ratios of individual fit errors from noninteractive spectral fitting to the Q uncertainty computed from MC simulations (i.e., Fit_err/Q), for each of the sources that were included in the comparison analysis (see Section 5.1). Error ratios were computed for the three main parameters, NH, kT, and unabsorbed flux. Gray crosses are the individual source Fit_err/Q ratios for combined positive and negative uncertainties, with errors representing 1σ uncertainties. Small green and blue circles correspond to the forward-moving averages (see text for description) as a function of the increasing background fraction for positive and negative 1σ quantiles, respectively. Small red circles were computed in the same way but assuming both positive and negative quantile distributions as a single one. Bottom: simply histograms taken on the y-axis (mean Fit_err/Q) of the corresponding set of colored points in the top panels.

The ratio between these two quantities is shown as gray crosses in Figure 7 (top panels).

In order to give a robust quantitative estimate of the reliability of our method, we made use of a statistical estimator known as the forward-moving average (FMA), which can be computed from the cumulative unweighted averages of a given set of sorted sample data points. We sort all the fit_err/Q values in ascending order of background fraction. The FMA starts from the first fit_err/Q value until the next recomputed current $(n+1)$ value, to the last adopted data point of our sample. Further details can be found from the help of the TS_SMOOTH[9] IDL task. We use this technique on parameters $N_{\rm H}$, kT, and unabsorbed X-ray flux to compute the goodness quantile error prediction with respect to the errors computed from X-ray spectral fits. As is shown in Figure 7, the majority of distributed FMA values are less than 10%–12%, even for higher background fractions.

While the combined positive and negative uncertainties from our approach are in excellent agreement with uncertainties from spectral fits to observed data, we note that the one-sided uncertainties do show some systematic deviations, albeit at levels of only 10% or so. This is revealed by the spread in the colored circles in the top panels of Figure 7 and in the separation of the distributions in the bottom panels. There are good reasons why the uncertainties should *not* be in perfect agreement. Fits to observed data use only an approximation to the true instrument response—represented by the ARF and RMF files noted in Section 2—and also assume a spectral model that will diverge from the real emission spectrum of a plasma at some level. In contrast, the simulations are fit with exactly the same models used to generate them, such that the difference between the retrieved and input spectral parameters results from Poisson noise. In the regime of a large number of photon counts and relatively low background, these systematic differences will be more important.

Systematic errors in fitted spectral parameters due to "imperfect" instrument response functions and plasma model spectra will lead to systematic errors in the derived quantile because the point of interpolation in the 2D quantile maps will be offset from where it should ideally be. In regions of these maps that are relatively flat, this interpolation error will be small. However, there are some regions of these quantile planes that have larger gradients, and in these regions the systematic error in the derived quantile can be larger.

At the low-S/N end, we have also encountered in Section 3 the low hydrogen column density cases in which the spectral fit simulations are occasionally unable to constrain the lower bound $N_{\rm H}$ fit errors. Indeed, the discrepancy in the two-sided errors is largest for the unabsorbed flux, which in the bandpass of interest here is highly dependent on the uncertainty in $N_{\rm H}$.

[9] http://www.exelisvis.com/docs/TS_SMOOTH.html

The two-sided errors are somewhat more discrepant for unabsorbed flux than for the $N_{\rm H}$ absorption or kT plasma temperature, which are in excellent agreement. Chandra ACIS-I spectra have good observational leverage on plasma temperature for typical Cyg OB2 sources. However, modeling degeneracies between $N_{\rm H}$ and kT are less well constrained for less absorbed stars with low-S/N spectra, potentially leading to inaccuracy in the error estimate for the unabsorbed flux. In light of this discussion, we conclude that in general the error estimation from spectral fitting is in very good agreement with our quantile estimates. Our method then represents a reliable means for error estimation in X-ray spectral parameters whenever the model fit to the X-ray data cannot provide it, as well as for observation planning in which data are not yet in hand. The method can also be applied to promptly estimate the errors in spectral parameters for previously studied X-ray source populations when uncertainties where not published or are otherwise unavailable.

6. Summary

In Figures 8–13 we present a new method for the estimation of errors in X-ray spectral parameters and fluxes of faint sources detected by ACIS-I on board Chandra. X-ray sources in the range of 10–350 net photons are generally not well suited to quantitative spectral analysis. Simple X-ray spectral modeling of such weak sources can suffer from ill-constrained solutions and mismatches between true and modeled parameters, combined with unrealistic estimation of the true uncertainties.

Here we have described an original treatment that resolves these problems by means of an extensive set of MC simulations of faint X-ray spectra. As representative cases, we adopted absorbed optically thin thermal plasma models and power-law continua that are commonly employed to interpret a wide range of astrophysical sources of X-rays. We fitted simulated spectra for a wide range of absorption, plasma temperature, and power-law index. We studied the relative error distributions of retrieved parameters and fluxes and described fits in terms of 1σ quantiles. We computed parametric curves of quantiles as a function of given input model parameters and interpolated within these to compute bidimensional maps. Such a set of maps provides an estimation of the true error in spectral parameters whenever it is not possible to determine these adequately from a direct spectral fit.

Our method makes it possible to improve statistical studies of objects in which a large fraction have a low number of counts. As an example, we have applied this method to sources in the Chandra Cygnus OB2 Legacy Survey and the properties of faint X-ray sources that mostly correspond to young low-mass stars. The uncertainties estimated using the quantile method presented here and from spectral fitting applied to the observations are in excellent agreement and generally at a level of 10% or better.

Finally, our method and data enable the computation of the exposure times required for surveys and individual pointed observations to reach a given uncertainty in derived spectral parameters. The results of this work will be made publicly available in an online tool in the near future.

Acknowledgments

We thank the referee Dr. Maurice Leutenegger for many very helpful suggestions to our article. J.F.A.-C. is a researcher of CONICET and the University of Rio Negro (UNRN) and acknowledges support from grant CONICET in the context of an external postdoctoral fellowship at the Osservatorio Astronomico di Palermo (OAPA). E.F. acknowledges support from the INAF and to the OAPA. J.J.D. and V.K. were supported by NASA contract NAS8-03060 to the Chandra X-ray Center (CXC) and thank the director, B. Wilkes, and the science team for continuing support and advice.

Appendix

All maps and calculation tools behind this section can be used in the Chandra ACIS Monte Carlo Photon Estimator Recipe calculation tool at http://camper.lia.unrn.edu.ar/.

Figures 8–13 present bidimensional maps of the Q uncertainty for flux and spectral parameters of thermal and nonthermal models. As examples, we show 2D quantile maps restricted to 90–100 X-ray photons in the simulated spectra. See the captions for a description of individual panels. All coefficients for uncertainty estimation at different photon statistics are listed in Tables 2–7. For each case, movies covering all ranges of parameters investigated as a function of the X-ray net counts in the spectra are presented as online material and are available at http://camper.lia.unrn.edu.ar/.

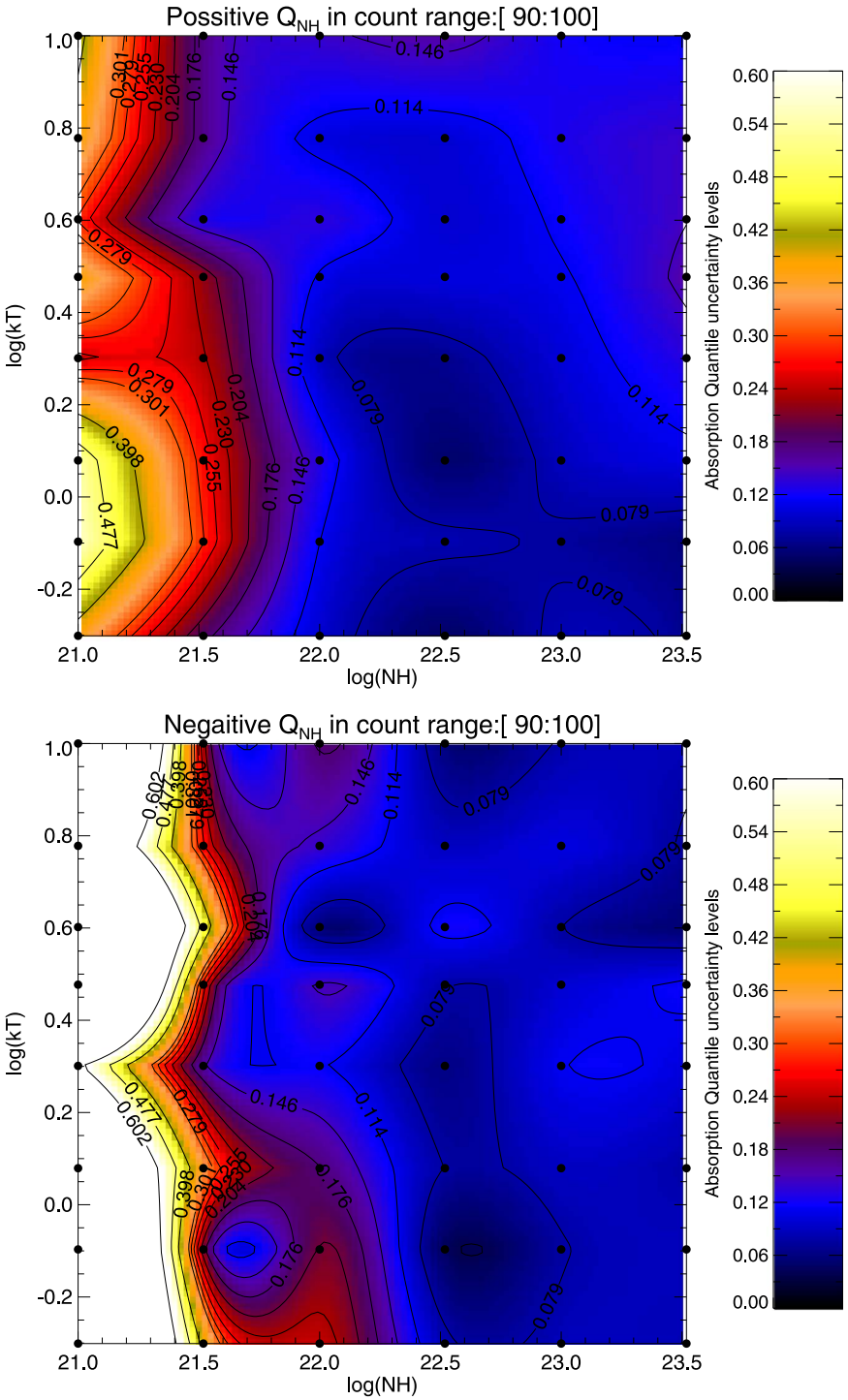

Figure 8. 2D–$N_{\rm H}$ example quantile maps from simulations of thermal models with 90–100 net photon counts. Left and right columns refer to positive and negative 1σ quantiles, respectively. The complete movie of the quantile map covering the full range of net count of photons in simulated spectra is presented as online material. (An animation of this figure is available.)

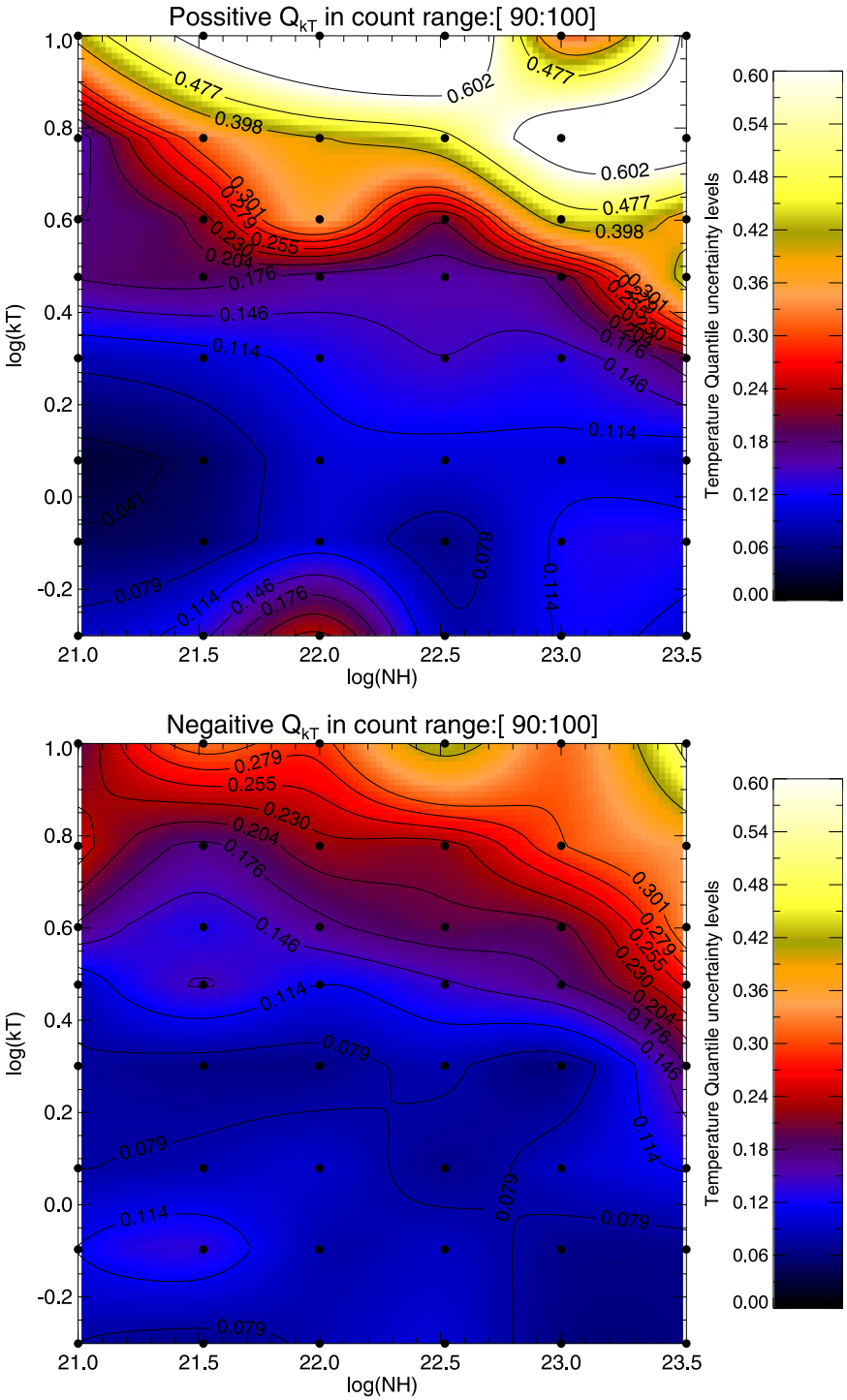

Figure 9. 2D–temperature example quantile maps from simulations of thermal models with 90–100 net photon counts. Left and right columns refer to positive and negative 1σ quantiles, respectively. The complete movie of the quantile map covering the full range of net count of photons in simulated spectra is presented as online material.

(An animation of this figure is available.)

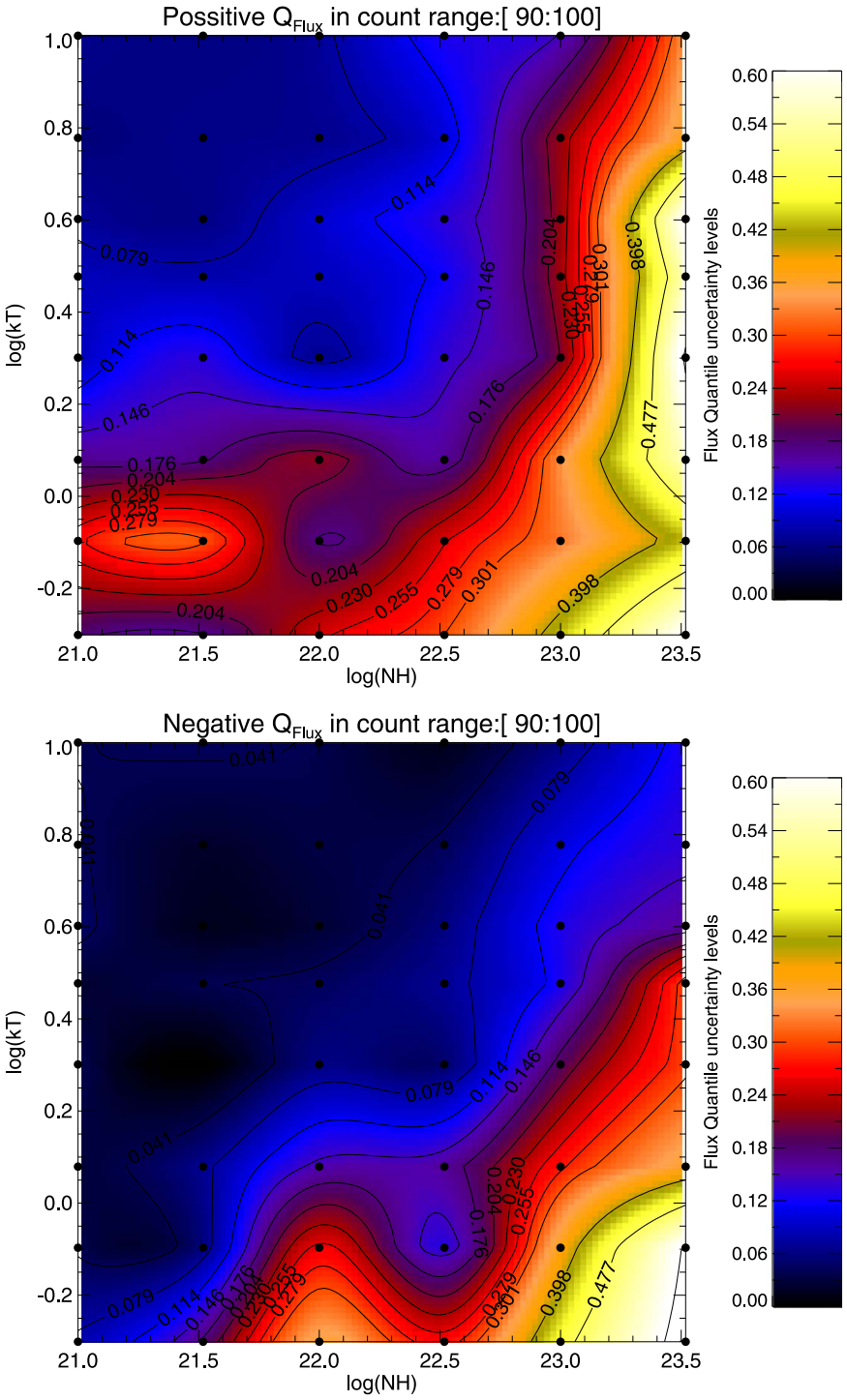

Figure 10. 2D–flux example quantile maps from simulations of thermal models with 90–100 net photon counts. Left and right columns refer to positive and negative 1σ quantiles, respectively. The complete movie of the quantile map covering the full range of net count of photons in simulated spectra is presented as online material. (An animation of this figure is available.)

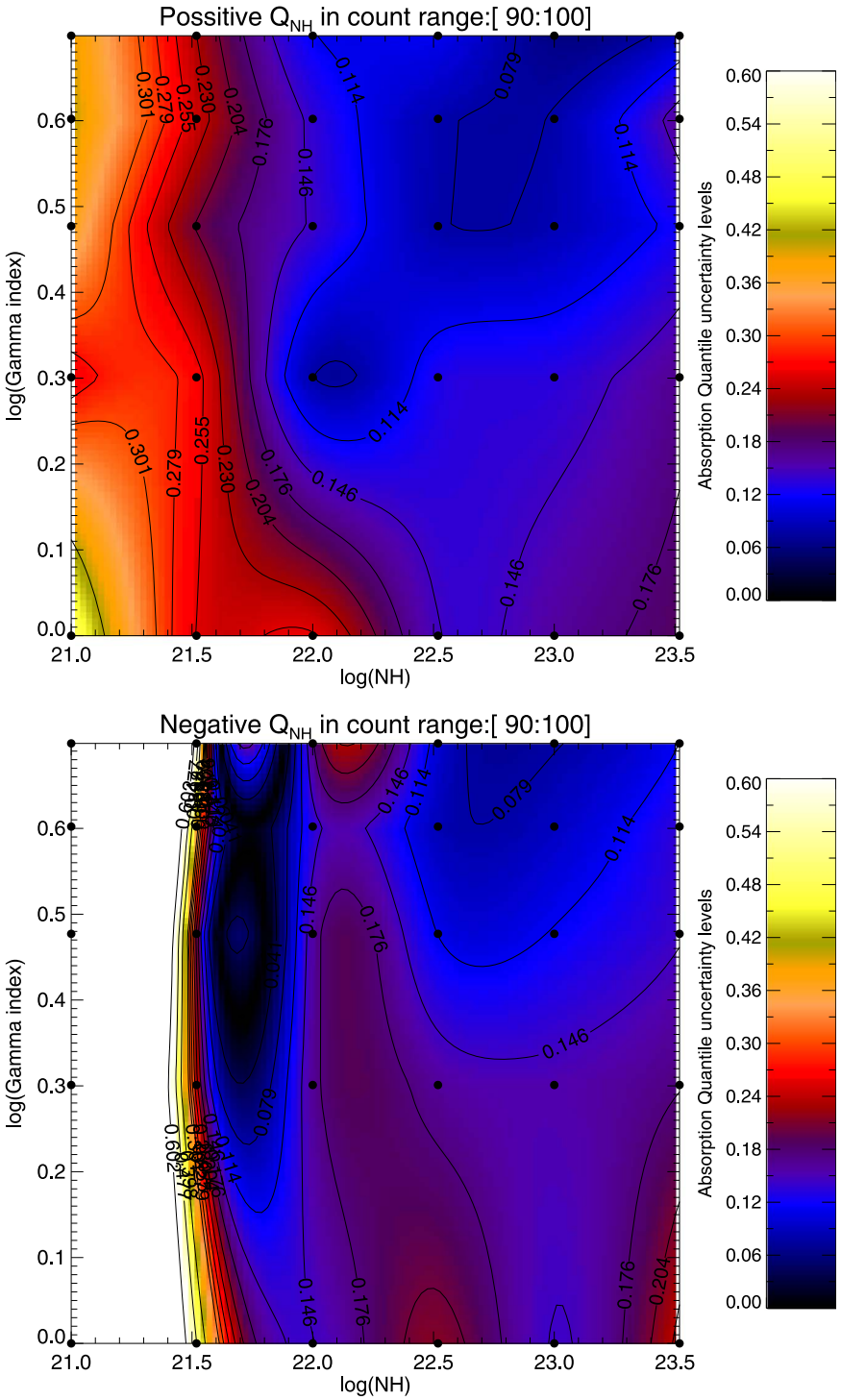

Figure 11. 2D–N_H example quantile maps from simulations of nonthermal models with 90–100 net photon counts. Left and right columns refer to positive and negative 1σ quantiles, respectively. The complete movie of the quantile map covering the full range of net count of photons in simulated spectra is presented as online material.

(An animation of this figure is available.)

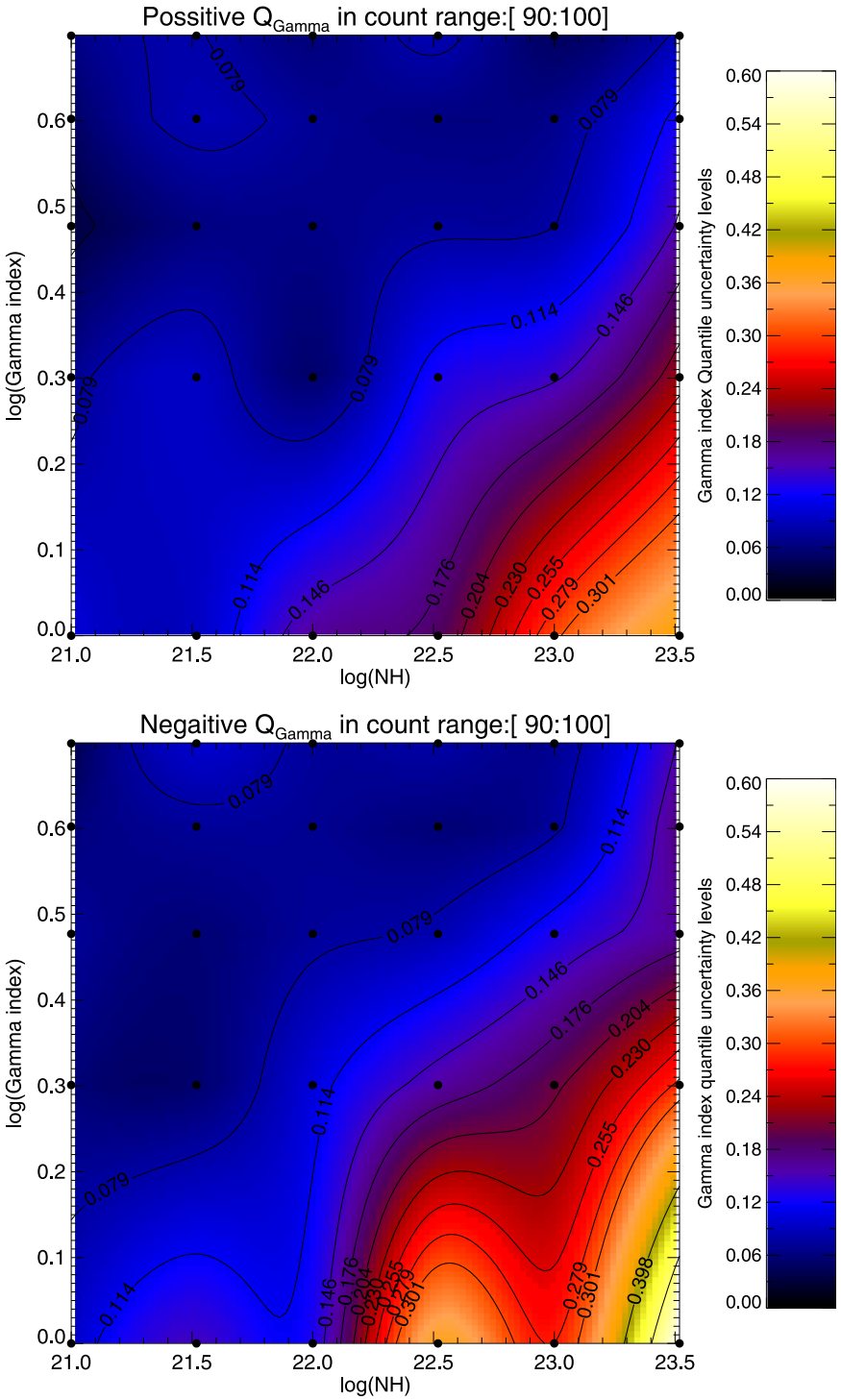

Figure 12. 2D–Γ index example quantile maps from simulations of nonthermal models with 90–100 net photon counts. Left and right columns refer to positive and negative 1σ quantiles, respectively. The complete movie of the quantile map covering the full range of net count of photons in simulated spectra is presented as online material.

(An animation of this figure is available.)

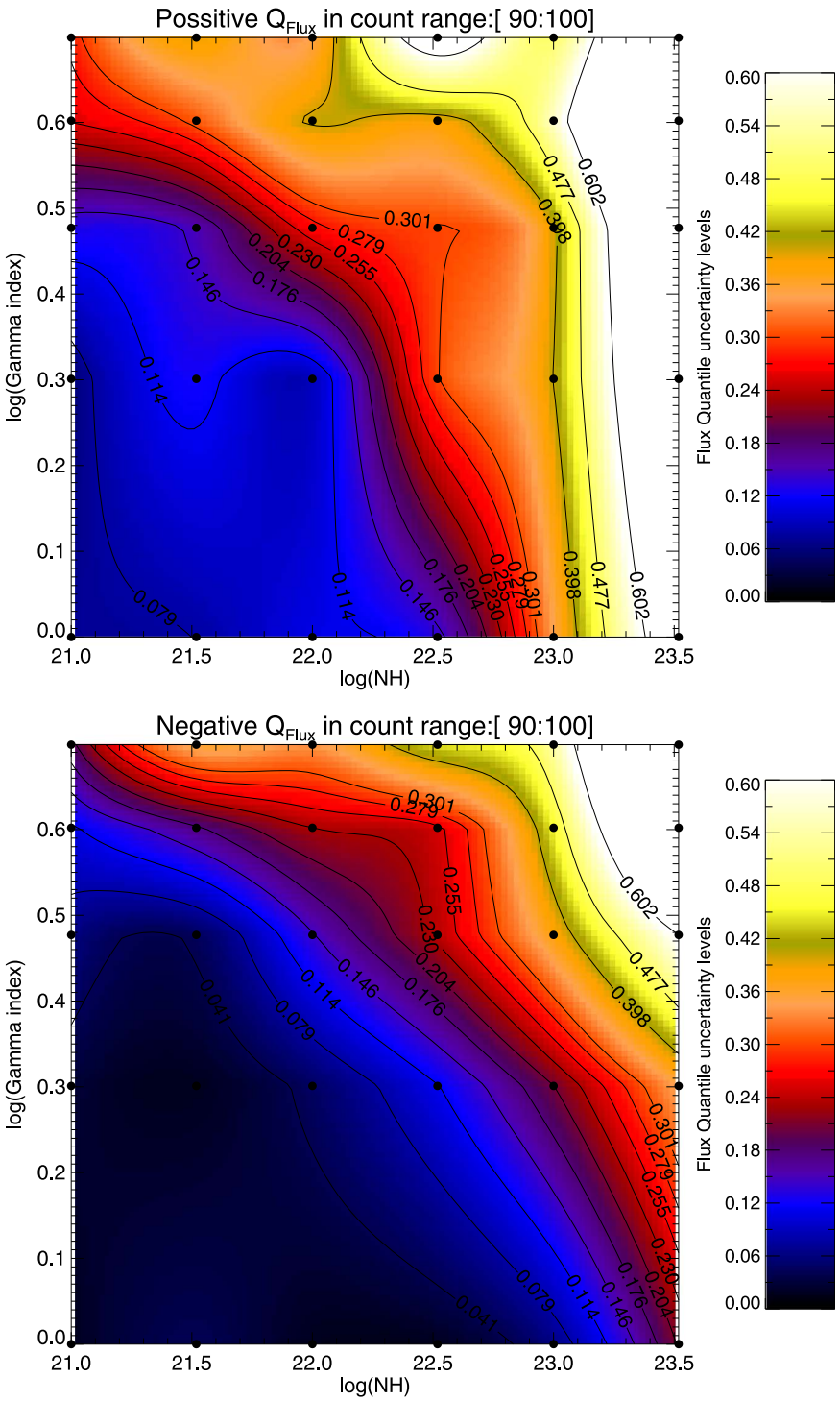

Figure 13. 2D–flux example quantile maps from simulations of nonthermal models with 90–100 net photon counts. Left and right columns refer to positive and negative 1σ quantiles, respectively. The complete movie of the quantile map covering the full range of net count of photons in simulated spectra is presented as online material.

(An animation of this figure is available.)

Table 2
Coefficients for Correction of the Absorption (N_H) Q Uncertainty in Terms of the Background Contamination Fraction for a Thermal X-Ray Source Model

Model	20 Photons	30 Photons	100 Photons	300 Photons
1	0.56999999, −0.79058786	0.29294601, −0.35787199	0.18000001, −0.32236677	0.11482079, −0.087020800
2	1.5800000, −1.5800000	0.43000001, −0.43000001	0.18000001, −0.18000001	0.029938766, −0.029938766
3	1.0000000, −1.0000000	0.59519789, −0.59519789	0.11634470, −0.11634470	0.10000000, −0.10000000
4	0.049715455, −1.0000000	0.62929869, −3.2919384	0.12753756, −0.41111881	0.00016174661, −0.17443736
5	0.11171015, −0.61089794	0.079572385, −0.52813251	0.079557867, −0.11617288	0.043629286, −0.044922529
6	1.3000000, −2.0934750	0.67000002, −0.75529767	0.093786779, −0.25956268	0.086018041, −0.057652803
7	0.88999999, −0.57335823	0.27781488, −0.44000000	0.18754265, −0.062686584	0.16403699, −0.039999999
8	0.58999997, −0.60203861	0.41679498, −0.35140125	0.42944980, −0.12969924	0.28124141, −0.022691981
9	0.87000000, −0.87000000	0.49000001, −0.49000001	0.23999999, −0.23999999	0.11832534, −0.11832534
10	0.38999999, −0.790000	0.27743047, −0.440000	0.063187085, −0.28924141	0.034755657, −0.029999999
11	0.63999999, −0.64599982	0.10191273, −0.61887488	0.11436878, −0.18611558	0.030987269, −0.11433628
12	0.38999999, −0.69138395	0.28999999, −0.37843546	0.21054822, −0.20999999	0.067875243, −0.19371328
13	0.58999997, −0.69999999	0.50999999, −0.57290317	0.44196881, −0.10809053	0.23690649, −0.088281814
14	1.0000000, −1.0000000	0.23863081, −0.23000000	0.16731354, −0.096115480	0.029999999, −0.087420713

Table 3
Coefficients for Correction of the Temperature (kT) Q Uncertainty in Terms of the Background Contamination Fraction for a Thermal X-Ray Source Model

Model	20 Photons	30 Photons	100 Photons	300 Photons
1	1.1791490, −0.69999999	1.0236216, −0.38275211	0.35172140, −0.16000000	0.070000000, −0.12034473
2	0.59865859, −0.40000001	0.15000001, −0.22137435	0.079999998, −0.10181730	−0.0058132137, −0.020912962
3	1.6737583, −1.0000000	0.40438804, −0.67145439	0.25332680, −0.12570339	0.080397019, −0.032017613
4	1.5045421, −0.19886096	1.0100729, −0.70493358	0.35332554, −0.19089511	0.12219090, −0.064251043
5	1.0285405, −0.22003141	1.3540962, −0.14531649	0.16706693, −0.073932650	0.048124737, −0.019780164
6	1.7827508, −1.7827508	0.77129511, −0.77129511	0.13526567, −0.13457852	0.020276173, −0.14306573
7	1.9000000, −1.9000000	1.6500000, −1.6500000	1.3150349, −0.89999998	0.68300091, −0.15976273
8	1.6700000, −0.56000000	1.5449302, −0.46316759	0.43428638, −0.35728049	0.12876973, −0.17824362
9	1.1222106, −0.33227760	1.1170738, −0.14316164	0.38273876, −0.072976206	0.058509901, −0.092050602
10	0.98000002, −0.44000000	0.68061929, −0.27748997	0.54441994, −0.16165912	0.21343224, −0.15936723
11	0.68000001, −0.68000001	0.55418089, −0.19408860	0.69571872, −0.22827677	0.13584275, −0.12354602
12	1.7900000, −0.28999999	1.3700000, −0.25924568	1.2029648, −0.14825462	0.36546867, −0.050000001
13	1.90000, −0.70999998	1.70000, −0.52999997	1.5044654, −0.41568087	0.48996156, −0.33525367
14	1.14000, −0.63999999	0.990000, −0.34000000	0.80259332, −0.19586915	1.2665589, −0.15802399

Table 4
Coefficients for Correction of the Unabsorbed Flux (Flux) Q Uncertainty in Terms of the Background Contamination Fraction for a Thermal X-Ray Source Model

Model	20 Photons	30 Photons	100 Photons	300 Photons
1	0.600000, −0.330000	0.54025202, −0.11000000	0.10682827, −0.050495573	0.040233470, −0.036603905
2	0.60000002, −0.22000000	0.26444894, −0.075128038	0.14690279, −0.035009770	0.0088736486, −0.0088736486
3	0.61000001, −0.330000	0.46442869, −0.022708227	0.091840132, −0.074119511	0.033806779, −0.041856700
4	0.32547463, 0.22537710	0.71408237, −0.0064318752	0.094341279, −0.068698972	−0.0054402611, −0.019880270
5	0.63611881, −0.58999997	0.38808347, −0.36155323	0.21717026, −0.21975059	0.16171609, −0.074638882
6	0.69999999, −0.69999999	0.55000001, −0.55000001	0.23215765, −0.097066930	0.15446032, −0.041110827
7	1.8000000, −1.8000000	1.3300000, −1.3300000	0.62809720, −0.20183422	0.38454859, −0.19000000
8	1.8800000, −0.49000001	1.6358418, −0.24090247	0.83024481, −0.15000001	0.28627373, −0.12124413
9	0.33069971, −0.33069971	0.22148313, −0.22148313	0.077915734, −0.062867283	0.024395005, −0.040764767
10	0.38207975, −0.38999999	0.28651545, −0.070000000	0.072748663, −0.029204307	0.020000000, −0.063466439
11	0.27969115, −0.27969115	0.20694499, −0.060739656	0.086205055, −0.049771037	0.00058630777, −0.068272805
12	0.38270376, −0.38999999	0.29421943, −0.27000001	0.12630442, −0.19000000	0.029999999, −0.13910898
13	0.900000, −0.41000000	0.770000, −0.28565844	0.63059201, −0.060723811	0.23391268, −0.070676279
14	1.3000000, −1.3000000	0.60592199, −0.80000001	0.51963257, −0.23999999	0.039999999, −0.15035874

Table 5
Coefficients for Correction of the Absorption (N_H) Q Uncertainty in Terms of the Background Contamination Fraction for a Nonthermal X-Ray Source Model

Model	30 Photons	100 Photons	300 Photons
1	0.25650181, −1	0.12430397, −0.50202637	0.18169266, −1.1245344
2	0.40523864, −0.30208423	0.11622960, −1.1318363	0.28298807, −2.9794969
3	0.22044614, −1	0.55048480, −0.051447758	0.52473601, −3.2887644
4	0.500000, −4.6345525	0.16597746, −0.97468140	0.066336864, −0.31664817
5	0.12215644, −0.79181550	0.10350067, −0.29293987	0.074220414, −0.16425698
6	0.089567717, −1.0198450	0.23257742, −0.25237991	0.096013813, −0.17154169
7	0.570000, −0.250000	0.57413525, −0.34905480	0.37936515, −0.28201250
8	0.27773648, −1.2329168	0.36234157, −0.15427702	0.19328749, −0.14761850

Table 6
Coefficients for Correction of the Gamma Index (Γ) Q Uncertainty in Terms of the Background Contamination Fraction for a Nonthermal X-Ray Source Model

Model	30 Photons	100 Photons	300 Photons
1	0.19699650, −0.081710183	0.052672355, −0.093241764	0.039347859, −0.050306389
2	0.25117132, −0.10266247	0.078957645, −0.067741463	0.038052451, −0.060455948
3	0.21329448, −0.016207271	0.22695826, −0.010517673	0.16103488, −0.046310364
4	0.400000, −0.500000	0.097128085, −0.33579614	0.0047083283, −0.23929186
5	0.082105410, −0.29366887	0.091130471, −0.13137739	0.040882831, −0.059770894
6	0.12310893, −0.28904541	0.22853133, −0.14899948	0.10236678, −0.12266170
7	1.50000, −0.600000	0.800000, −0.500000	0.35792970, −0.52635195
8	0.43658025, −0.49066309	0.16724924, −0.19066881	0.067044326, −0.043196329

Table 7
Coefficients for Correction of the Unabsorbed Flux (Flux) Q Uncertainty in Terms of the Background Contamination Fraction for a Nonthermal X-Ray Source Model

Model	30 Photons	100 Photons	300 Photons
1	0.17029916, −0.027228378	0.053110142, −0.043069600	0.027653891, −0.025060421
2	1.0406915, 0.012650287	0.077507279, −0.039221376	0.073060202, −0.035090637
3	0.77695532, 0.013296297	0.90757450, −0.062870060	0.53249562, −0.12403132
4	0.23904451, −0.040587606	0.048288826, −0.046017530	0.0500000, −0.041524861
5	0.58708610, −0.093046929	0.31389033, −0.23559708	0.12070400, −0.12857378
6	0.540000, −0.55078238	1.3023024, −0.51431365	0.41070973, −0.56508111
7	1.1208722, −0.10905732	1.1694971, −0.072869982	0.38194822, −0.13259251
8	2.2073709, −0.56064182	1.1706366, −0.44397279	0.40848299, −0.30326180

ORCID iDs

J. F. Albacete-Colombo https://orcid.org/0000-0001-8398-0515
E. Flaccomio https://orcid.org/0000-0002-3638-5788
J. J. Drake https://orcid.org/0000-0002-0210-2276
M. Guarcello https://orcid.org/0000-0002-3010-2310
V. Kashyap https://orcid.org/0000-0002-3869-7996

References

Albacete Colombo, J. F., Flaccomio, E., Micela, G., Sciortino, S., & Damiani, F. 2007, A&A, 464, 211
Anders, E., & Grevesse, N. 1989, GeCoA, 53, 197
Arnaud, K. A. 1996, in ASP Conf. Ser. 101, Astronomical Data Analysis Software and Systems V, ed. G. H. Jacoby & J. Barnes (San Francisco, CA: ASP), 17
Broos, P. S., Townsley, L. K., Feigelson, E. D., et al. 2010, ApJ, 714, 1582
Cash, W. 1979, ApJ, 228, 939
Flaccomio, E., Albacete-Colombo, J. F., Drake, J. J., et al. 2023, ApJS, 269, 12
Guarcello, M. G., Drake, J. J., Wright, N. J., et al. 2023, ApJS, 269, 9
Hong, J., Schlegel, E. M., & Grindlay, J. E. 2004, ApJ, 614, 508
Kashyap, V. L., Guarcello, M. G., Wright, N. J., et al. 2023, ApJS, 269, 10
Maggio, A., Sciortino, S., Collura, A., & Harnden, F. R., Jr 1995, A&AS, 110, 573
O'Dell, S. L., Swartz, D. A., Tice, N. W., et al. 2013, Proc. SPIE, 8859, 88590F
Smith, R. K., Brickhouse, N. S., Liedahl, D. A., & Raymond, J. C. 2001, ApJL, 556, L91
Wright, N. J., Drake, J. J., Guarcello, M. G., et al. 2023a, ApJS, 269, 7
Wright, N. J., Drake, J. J., Guarcello, M. G., Kashyap, V. L., & Zezas, A. 2023b, ApJS, 269, 8